HOSTED BY

ELSEVIER

CrossMark

Available online at www.sciencedirect.com

ScienceDirect

Progress in Natural Science: Materials International 24 (2014) 599–607

Progress in Natural Science Materials International

www.elsevier.com/locate/pnsmi
www.sciencedirect.com

Original Research

Microstructural study and numerical simulation of phase decomposition of heat treated Co–Cu alloys

A.M. Mebed[a,b,*], Alaa M. Abd-Elnaiem[a]

[a]Department of Physics, Faculty of Science, Assiut University, Assiut 71516, Egypt
[b]Department of Physics, Faculty of Science, Aljouf University, Sakaka 2014, Saudi Arabia

Received 8 February 2014; accepted 1 October 2014
Available online 4 December 2014

Abstract

The influence of heat treatment on the phase decomposition and the grain size of Co–10 at% Cu alloy were studied. Few samples were aged in a furnace for either 3 or 5 h and then quenched in iced water. The materials and phase compositions were investigated using energy dispersive spectrometry and X-ray diffraction techniques. X-ray diffraction analysis showed that the samples contained Co, Cu, CuO, $CoCu_2O_3$, $CoCuO_2$ phases in different proportions depending on the heat treatment regimes. The formation of dendrite Co phase rendered the spinodal decomposition while the oxidations prevent the initiation of the spinodal decomposition even for a deep long aging inside the miscibility gap. Since the Bragg reflections from different phases of Co–Cu alloy significantly overlap, the crystal structural parameters were refined with FULLPROF program. The shifts in the refined lattice constants (a, b and c), the space group and the grain size were found to be phase- and heat treatment-dependant. Two-dimensional computer simulations were conducted to study the phase decomposition of Co–Cu binary alloy systems. The excess free energy as well as the strain energy, without a priori knowledge of the shape or the position of the new phase, was precisely evaluated. The results indicate that the morphology and the shape of the microstructure agree with SEM observation.

Keywords: Co–Cu alloys; Phase decomposition; X-Ray diffraction; Rietveld analysis; Computer simulation

1. Introduction

Co–Cu alloys are important materials for various applications including magneto-resistivity and ferromagnetism [1,2], chemical sensing [3] and coating technology [4]. An aspect of Co–Cu systems that has been well studied for the past decades is their mechanisms of phase transition [5–10]. These mechanisms are spinodal decomposition [11,12], nucleation-growth [13], and growth by grain boundary diffusion [14]. Heat treatments (such as annealing and quenching) have been used to modify the properties of these alloys through homogeneous precipitation due to spinodal phase decomposition. In addition, their performances have been enhanced by changing the grain size and phase distribution [15,16].

Phase compositions in multiphase alloys can be quantified by X-ray diffraction (XRD) technique. However, due to significant overlapping of Bragg reflections for Co–Cu alloys, the possibility of texture effect becomes more dominant and accuracy of phase

Abbreviations: T, Absolute temperature; r, Crystal lattice position and its time derivative (r' and r''); p, Position vector for the lattice points, and its derivatives (p' and p''); t, Time; $c(\mathbf{r},t)$, Occupation probability of finding a solute atom at position $\mathbf{r}$ in time t; $c(\mathbf{p},t)$, Occupation probability of finding a solute atom at position $\mathbf{p}$ in time t; c_0, Average composition; $L(\mathbf{r}-\mathbf{r}')$, Matrix of kinetic coefficients related to probabilities of elementary diffusional jumps from lattice site $\mathbf{r}$ to $\mathbf{r}'$ of a Bravais lattice; $W\{\mathbf{p}'-\mathbf{p}'', c(\mathbf{p}'), c(\mathbf{p}''), T\}$, Function of a pair wise interaction energy between atoms, at interatomic distance $(\mathbf{p}'-\mathbf{p}'')$; $W^{str}\{\mathbf{r}'-\mathbf{r}'', c(\mathbf{r}'), c(\mathbf{r}''), T\}$, Strain – induced interaction; G_c, Chemical free energy; E_{str}, Elastic strain energy; G_T, Total free energy; ε, Eigen strain, η is the lattice mismatch; K_B, Boltzmann constant; R, Gas constant; N_A, Avogadro's number; h, Fourier wave number; L, Length of calculation field in real space; N, Maximum number of h; $Q_1(\mathbf{h})$, Fourier transform of $c(\mathbf{r})$; $Q_{j+1}(\mathbf{h})$, j[th] evolution of $Q_1(\mathbf{h})$; $V_j(\mathbf{h})$, Fourier transform of $W_j\{\mathbf{r}'-\mathbf{r}''\}$; $B(\mathbf{h})$, Fourier transform of $W_{str}\{\mathbf{r}'-\mathbf{r}''\}$; $M(\mathbf{h})$, Fourier transform of $L\{\mathbf{r}-\mathbf{r}'\}$; Δt, Time interval; C_{ijkl}, Elastic stiffness constant; F, Helmholtz free energy; h_x *and* h_y, Directional components of the wave vector $\mathbf{h}$; c_α, Atomic fraction of atoms of kind α

*Corresponding author currently at: Department of Physics, Faculty of Science, Aljouf University, Sakaka 2014, Saudi Arabia.
Tel.: +966 553348704; fax: +966 6247183.
E-mail address: abdu_55@yahoo.com (A.M. Mebed).

Peer review under responsibility of Chinese Materials Research Society.

http://dx.doi.org/10.1016/j.pnsc.2014.10.001

quantification diminishes. An alternative method for structure refinement is the Rietveld method (RM) [17–22]. RM eliminates peaks overlapping by explicitly including all lines for each phase in the refinement. It also uses a reliable texture correction to minimize the undesirable effect of texture. More importantly, only knowledge of the phases and their respective crystal structures are needed [22]. RM is thus considered as a viable method for analyzing XRD spectra of our Co–Cu samples.

On the other hand, spinodal phase decomposition has been observed in some samples while the others not, even they all heat treated at the same conditions deeply inside the miscibility gap. For the best of our knowledge, no explanations for that phenomenon can be found in previous works. Moreover, phase quantification in Co–Cu system using RM is rare. Therefore, this paper reports a systematic experimental technique designed to reveal the effect of oxidation and the other phases on the initiation of spinodal or binodal decomposition. To obtain an accurate value of the grain size a correction for the instrumental broadening is considered in the present work.

It has been established that phase decomposition in multiphase alloy is controlled by the change in free energy of the system. For such a system, the combined effect of the bulk free energy, interfacial energy, as well as the elastic strain energy must be considered for a valuable treatment of the phase decomposition. Khachaturyan [23] pointed out that the strain energy of a two-phase mixture of an arbitrary morphology gives rise to a strain accommodation which results in a certain optimal microstructure. That accommodation is important in the later stage of the phase decomposition. Introducing additional free energy due to the formation of oxide interfaces prevent the formation of the mottled structure. Based on Refs. [23,24], we conducted two-dimensional (2D) computer simulations to study the phase decomposition of Co–10 at% Cu binary alloy system. We precisely evaluated the excess free energy as well as the strain energy without a priori knowledge of the shape or the position of the new phase. Thermodynamics data related to the equilibrium phase diagram of these systems were used. The calculated microstructures were compared to the experimental results.

2. Experimental

2.1. Sample preparation

Rod samples of Co–10 at% Cu alloys were synthesized from a mixture of pure Cu and Co pellets by means of the arc melting technique [14]. The samples were re-melted five times to enhance dispersion of Cu and Co particles. Small strips of about 1–2 mm thick were obtained for experimental study. Four samples were thermally treated in a quartz-glass tube under the same temperature and purified argon atmosphere but different aging times. The conditions were chosen to study the influence of thermal treatment on the quality and quantity of phases and grain/crystal in the samples. All samples were solid solution treated (SST) at a temperature of 1500 K and a heating rate of about 50 K/min. While sample S1 was thermally treated for 3 h, the others were treated for 5 h. All the samples (S1, S2, S3 and S4) were thermally aged according to the following conditions: S1 was aged in air at 1000 K for 10 min and then quenched in iced water. S2 and S3 were aged at 500 K for 5 h and 10 min in air, respectively, and then quenched in iced water. S4 was encapsulated in an evacuated quartz tube, aged at 1000 K for 10 min and then quenched in iced water.

The microstructures of the polished samples were observed by using JOEL-JSM-5400LV scanning electron microscopy equipped with energy dispersive spectrometry. The phases, crystal size and texture were investigated by X-ray diffraction techniques using a Phillips X-ray diffractometer with Cu K_α radiation. The spectra were acquired within the range of $2\theta = 40$–110° at a scanning step and a speed of 0.02° and $0.06\ ^\circ$/s, respectively. FULLPROF program was used to quantify the crystal phases. The optimized parameters for the refinements were background coefficients, displacement correction, peak shapes, and cell parameters. The residual values of the refinement, R-weighted pattern (R_{wp}), R-expected (R_{exp}), and goodness-of-fit (χ^2) were evaluated. The geometric structural parameters of the treated samples were determined from the refined lattice parameters while the crystal size was estimated from the modified Scherrer formula.

2.2. The kinetic model and time evolution

According to the previous study [19], the kinetic equation describing the time evolution of the occupation probability of finding an atom at crystal lattice position, $\mathbf{r}$, and at time, t, takes the form of the following equation:

$$\frac{\partial c(\mathbf{r},t)}{\partial t} = \sum_{\mathbf{r}'} \frac{L(\mathbf{r}-\mathbf{r}')c_0(1-c_0)}{RT}\left\{\frac{\delta G_T}{\delta c(\mathbf{r}',t)}\right\} \tag{1}$$

with

$$\begin{aligned}\frac{\delta G_T}{\delta c(\mathbf{r}')} = &\sum_j \frac{j+2}{2} c^{j+1}(\mathbf{p}') \sum_{\mathbf{p}''} W_j(\mathbf{p}'-\mathbf{p}'',T) \\ &+ \sum_{\mathbf{p}''} W_A(\mathbf{p}'-\mathbf{p}'',T)c(\mathbf{p}'') \\ &+ RT\sum_{\mathbf{p}'}[\ln c(\mathbf{p}') + \ln\{1-c(\mathbf{p}')\}] \\ &+ \sum_j \frac{j+2}{2} c^{j+1}(\mathbf{r}') \sum_{\mathbf{r}''} W_j^{str}(\mathbf{r}'-\mathbf{r}'',T) \\ &+ \sum_{\mathbf{r}''} W_A^{str}(\mathbf{r}'-\mathbf{r}'',T)c(\mathbf{r}'')\end{aligned}$$

Eq. (1) contains the contribution of the chemical free energy and that of the strain energy while the summation is carried out over all N lattice sites. Taking the Fourier transform of Eq. (1) the following equations result in:

$$\left\langle \frac{\partial c(\mathbf{r},t)}{\partial t} \right\rangle_h = \frac{1}{N^3}\sum_{\mathbf{r}} \left\{\frac{\partial c(\mathbf{r},t)}{\partial t}\right\} \exp(-ih\beta\mathbf{r}) = \frac{\partial Q_1(h,t)}{\partial t} \tag{2}$$

$$\left\langle \frac{c_0(1-c_0)}{RT} \sum_{\mathbf{r}'} L(\mathbf{r}-\mathbf{r}')\left\{\frac{\delta G_T}{\delta c(\mathbf{r}',t)}\right\} \right\rangle_h$$

$$= \frac{c_0(1-c_0)}{RT}\left(\frac{1}{N^3}\right)\sum_{\mathbf{r}} \left[\sum_{\mathbf{r}'} L(\mathbf{r}-\mathbf{r}')\left\{\frac{\delta G_T}{\delta c(\mathbf{r}',t)}\right\}\right] \exp(-ih\beta\mathbf{r})$$

$$= \frac{c_0(1-c_0)}{RT}\left(\frac{1}{N^3}\right)\sum_{\mathbf{r}}\left[\sum_{\mathbf{r}'}L(\mathbf{r}-\mathbf{r}')\left\{\frac{\delta G_T}{\delta c(\mathbf{r}',t)}\right\}\right]$$
$$\times\exp\{-ih\beta(\mathbf{r}-\mathbf{r}')\}\exp(-ih\beta\mathbf{r}') = \frac{c_0(1-c_0)}{RT}\left(\frac{1}{N^3}\right)$$
$$\times\sum_{\mathbf{r}'}\left[\sum_{\mathbf{r}-\mathbf{r}'}L(\mathbf{r}-\mathbf{r}')\exp\{-ih\beta(\mathbf{r}-\mathbf{r}')\}\right]\left\{\frac{\delta G_T}{\delta c(\mathbf{r}',t)}\right\}$$
$$\times\exp(-ih\beta\mathbf{r}') = \frac{c_0(1-c_0)}{RT}M(h)\left\langle\left\{\frac{\delta G_T}{\delta c(\mathbf{r}',t)}\right\}\right\rangle_h \quad (3)$$

where

$$M(h) = \sum_{r-\mathbf{r}'}L(\mathbf{r}-\mathbf{r}')\exp\{-ih\beta(\mathbf{r}-\mathbf{r}')\} \quad (4)$$

The mean field approximation is used to describe the main characteristics of the two-phase morphological evolution during precipitation reactions.

After Fourier transformation, Eq. (1) becomes:

$$\frac{\partial Q_1(\mathbf{h},t)}{\partial t} = \frac{c_o(1-c_o)}{RT}M(h)$$
$$\bullet\left[\sum_j\left\{\begin{matrix}\frac{j+2}{2}\left[V_j(\mathbf{h}\delta(\mathbf{h}))+B_j(\mathbf{h}\delta(\mathbf{h}))\right]+\\ [V_j(\mathbf{h})+B_j(\mathbf{h})]\delta(j)\{1-\delta(\mathbf{h})\}\end{matrix}\right\}Q_{j+1}(\mathbf{h})\right.$$
$$\left.+RT\left\{\ln\left(\frac{c(\mathbf{p}')}{1-c(\mathbf{p}')}\right)\right\}_h\right] \quad (5)$$

Where $\left\{\ln\left(\frac{c(\mathbf{p}')}{1-c(\mathbf{p}')}\right)\right\}_h$ is the Fourier transform of $\left\{\ln\left(\frac{c(\mathbf{p}')}{1-c(\mathbf{p}')}\right)\right\}$

The left-hand side of Eq. (5) can be defined and the time developments of $Q_1(\boldsymbol{h},t)$ can be evaluated in the do-loop of Eq. (6).

$$Q_1(\mathbf{h},t+\Delta t) = Q_1(\mathbf{h},t)+\left(\frac{\partial Q_1}{\partial t}\right)_t\Delta t \quad (6)$$

The back Fourier transforms obtained from Eq. (6) give the occupation probabilities $c(\boldsymbol{r},t)$. Representation of the occupation probabilities in two dimensions give quit good prediction of the shapes, habits, concentration profiles, as well as mutual distributions of the precipitates. More details about system model and simulation technique are available elsewhere [19].

3. Results and discussion

3.1. EDS and SEM characterization

Fig. 1 shows the EDS chart and the SEM image for the as-prepared Co–10 at% Cu alloy. The EDS chart exhibits peaks correspond to Co and Cu elements. The Co and Cu contents of the alloy were calculated using the *k*-factor of each element [25]. The k-factors were determined from the ratio of the *k*-alpha peak intensities for Cu and Co obtained from the EDS at the start of the analysis and those of known alloy composition [26]. Co was found to form, on average of 95 at%, while the Cu contribution was found to be 5 at% in all the thermal treated samples. In spite of the large difference between the expected and the actual compositions, this result is not surprising since alloy suffers from the phase decomposition during the heat treatment process. The as-prepared Co–10 at% Cu sample had a typical cast microstructure as shown in Fig. 1b. The shape of the Co-rich phase appeared irregular but more of oblong shape. The average size of the Co-rich phase was about 40 μm. Co/Co grain boundaries (GBs) were visible and the grains appear light-grey. The Cu rich solid solution phase appeared dark-grey and forms chains along the Co/Co GBs. In this case, the Cu solid solution formed the continuous layer separating the Co grains. Due to the binodal phase decomposition most of the Cu atoms in the Co-rich phase (for the as-prepared samples) moved into the chains of Cu-rich phase by occupying the Co/Co boundary. After 5 h of aging of sample S4, the Cu atoms migrated from the previously noticed Cu-rich chain to the Co dendrite phase. The reduction in the volume of the Cu-rich phase is attributed to the decomposition of the alloy to a richer Co phase by heterogeneous nucleation at the grain boundaries and grain-boundary diffusion by binodal decomposition Fig. 2a. It is also clear that the phase separation process and microstructures are controlled by the

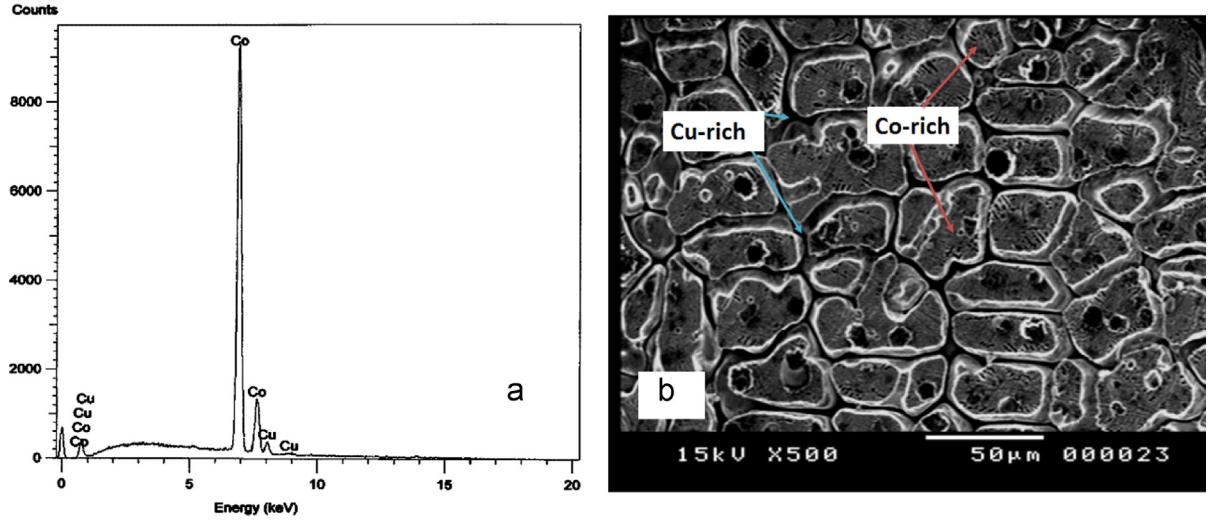

Fig. 1. (a) EDS chart and (b) SEM image of the as-prepared Co–10 at% Cu alloy.

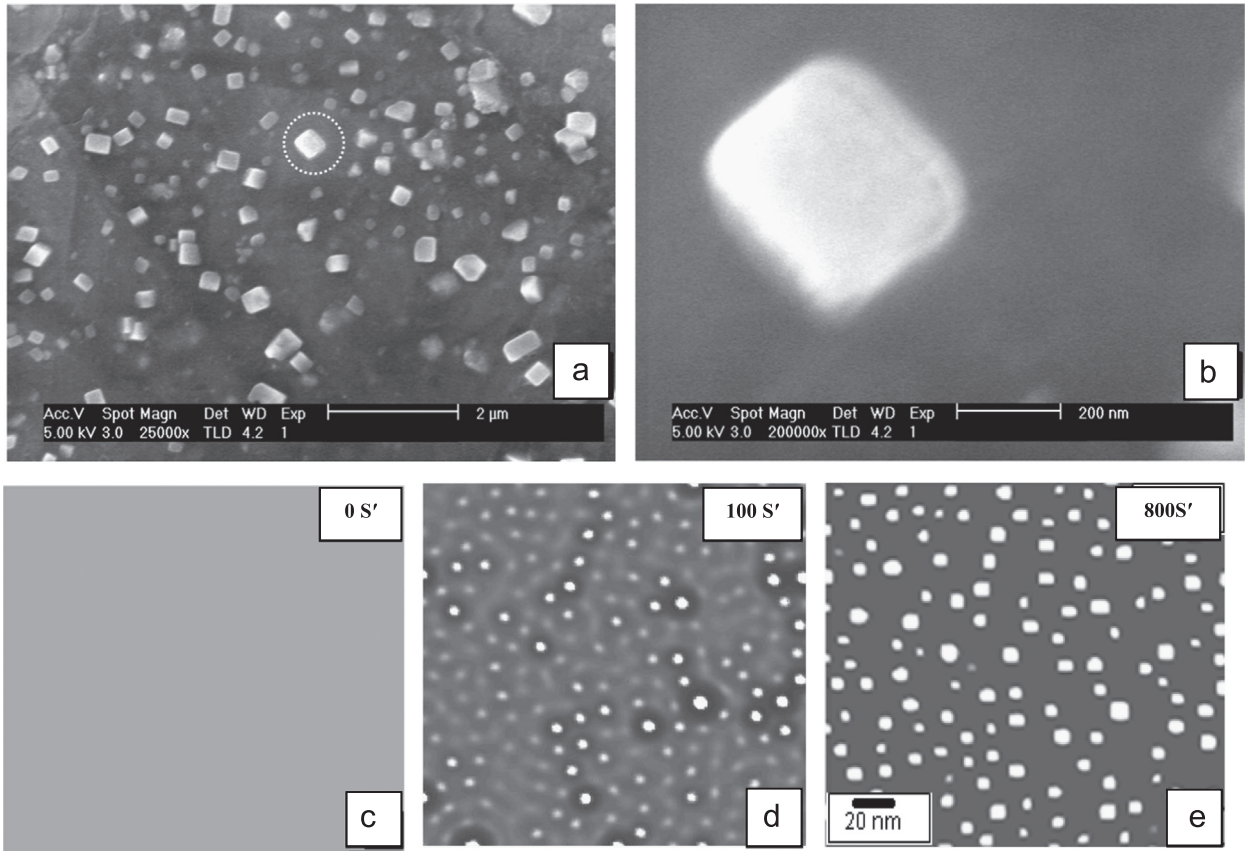

Fig. 2. SEM images of the heat treated Co–10 at% Cu alloys: (a) Cu rich phase of S4 with Co particles, (b) a single cubic Co particle with dimensions of 200 nm, (c) Cu rich phase as a solid solution with composition Cu–10 at% Co as an initial state of computer simulation, (d and e) 2D computer simulation of Fig. 2c after 100 s and 800 s, respectively.

degree of aging, and the cooling rate. Fig. 2b shows the faceted Co particle after the Cu rich phase of sample S4 underwent binodal decomposition at 1000 K for 10 min.

3.2. Computational results

The atomic interchange energies of the Co–Cu system were determined from the following equation while other numerical values are listed in Table 1.

$$G_c = [\sum_j \Omega_j(T)c^j]c^2 + RT[c\ln(c) + (1-c)\ln(1-c)]$$
$$\Omega_0(T) = -60225 + 16.226T \quad (J/mol)$$
$$\Omega_1(T) = \quad 7150 - 1.9376T \quad (J/mol)$$
$$\Omega_j(T) = 0, \qquad j \geq 2 \qquad (7)$$

It is clear from Fig. 2d that the simulation started with the homogeneous solid solution with solute fluctuations. Hereafter, the chemical free energy drives the initial stage of the decomposition to form almost connected rounded shape particles. The particles were commonly coherent with the matrix. It is interesting to observe that, although the simulation was performed inside the spinodal region, it was lay near the nucleation growth region. That caused some particles to be larger in size than the others.

On aging, a coarsening process occurred. This modulated structure evolves from spinodal decomposition in elastically anisotropic cubic matrices, owing to the tendency to minimize the coherency strain energy to control the particle shape. Their shape is controlled by the rather complex interplay of various factors, such as the magnitude and anisotropy of the interfacial energy, the deference in the elastic constants between matrix and precipitates, and the crystal structure of the latter [23]. The elastic anisotropy parameter is positive rendering the minimum elastic energy along the elastically soft $< 100 >$ giving rise to modulated precipitate microstructures as shown from the experimental result Fig. 2a. In the 2D simulation, the particles were aligned along $\langle 10 \rangle$ or $\langle 01 \rangle$ directions since the elastic interaction energy among particles was essentially included in the present calculation. In this essence, the interplay between the interfacial energy and the elastic energy was recognized in the system of Co–Cu that is demonstrated in Fig. 2e. Fig. 2a and e have similar particle shape and distribution.

3.3. Rietveld method for phase identification

XRD spectra for the four samples are shown in Fig. 3. Although the spectra had the same feature, a change in the peak intensity and a slight shift in the peak positions were detected across the profiles. It is also clear from the profiles that not all the samples had the same phases. For example, a peak was located at $2\theta \approx 72^\circ$ for both samples S1 and S2

Table 1
Numerical values used for the calculations.

Parameter	Value
Ageing temperature (T/K)	873
Average solute composition (c_0)	0.06
Elastic stiffness of the matrix	
$C_{11}/10^4$/MN (m^{-2})	16.839
$C_{12}/10^4$/MN (m^{-2})	12.142
$C_{44}/10^4$/MN (m^{-2})	7.539
Lattice mismatch (η)	0.0196
Calculation area (L/nm)	60.0
Interaction Distance (d_1/nm)	0.868
Number of Fourier wave (N × N)	256 × 256

which correspond to CuO (222) but such a peak was absent for samples S3 and S4. More than one type of oxides, with different chemical compositions, was observed in the samples S1 and S2. The presence of these oxides is due to the incorporation of oxygen during aging process or partially during cooling process. CuO composition is not significantly giving its lower peak intensity compared to that of pure Co or Cu phase. The existence of a pure Cu metal phase in samples S3 and S4 at phase 2 is attributed to deep aging inside the miscibility gab forcing the Cu rich phase to decompose. The absence of oxidized Cu, Co or the combination thereof is due to the second stage treatment as well as the encapsulation in quartz tube. It is also observed that the preferred grow orientation for both Cu and Co phase is along the [111] direction.

To completely identify all the phases, we refined the XRD spectra with a Rietveld fitting method which has been incorporated into the FullProf fitting software [27]. The experimental spectra were fitted with the modified Thomson-Cox-Hasting pseudo Voigt functions [28]:

$$H = [H_G^5 + AH_G^4H_L + BH_G^3H_L^2 + CH_G^2H_L^3 + DH_GH_L^4 + H_L^5]^{0.2} \tag{8}$$

where A, B, C, and D are fitting parameters which are found to be 2.692, 2.428, 4.471 and 0.0782 respectively, and

$$H_G = \sqrt{U\tan^2\theta + V\ \tan\ \theta + W + \frac{Z}{\cos^2\theta}} \tag{9a}$$

$$H_L = X\ \tan\ \theta + \frac{Y}{\cos\ \theta} \tag{9b}$$

where H_G and H_L are the Gaussian and Lorentzian components of the peak, respectively. U/Z and X/Y are the isotropic micro-strain/crystallite size parameters for Gaussian and Lorentzian component, respectively. To perform a refinement, the back-ground noise due to the tool vibration was first removed. Then the structural parameters (specimen profile breadth parameters, lattice parameters and temperature factors) were refined. During the refinement, the weighted profile factor R_{wp}, the un-weighted profile factor R_p and the expected profile factor R_{exp} were monitored. These factors are expressed as given below

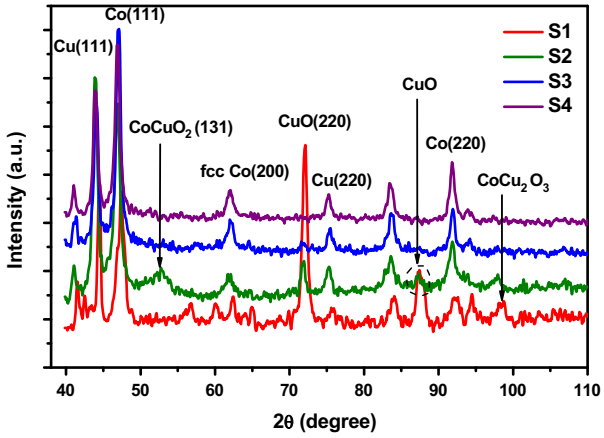

Fig. 3. XRD profiles for the samples under study. The indices of the most intense Bragg reflections are shown.

Table 2
Rietveld R-factors for Co–10 at% Cu alloy samples.

Sample	R_p	R_{exp}	R_{wp}	x^2
S1	15.2	20.5	22.25	1.178
S2	18.3	17.5	26.01	2.209
S3	21.1	20.2	30.74	2.315
S4	25.7	21.4	35.85	2.806

$$R_{wp} = 100\frac{\sqrt{w_i\left|\left(y_i - y_{c,i}\right)\right|^2}}{\sum_{i=1}^{n} w_i y_i^2} \tag{10a}$$

$$\frac{R_p = 100\sum_{i=1}^{n}\left|\left(y_i - y_{c,i}\right)\right|}{\sum_{i=1}^{n} y_i} \tag{10b}$$

$$R_{\exp} = 100\sqrt{\frac{n-p}{\sum_{i=1}^{n} w_i y_i^2}} \tag{10c}$$

The refinement was successful when all parameters converged to less than 10% of their standard deviations. At this point, all the parameters (global and structural) were refined simultaneously searching for a minimum goodness of fit indexχ^2. The goodness of fit, $\chi^2 = [\frac{R_{wp}}{R_{\exp}}]^2$, was then estimated from the converged values of R_{wp} and R_{exp}. The symbol $w_i = 1/\sqrt{y_i}$ wherey_i is the observed intensity (from the XRD measurement) at the step i, $y_{c,i}$is the calculated intensity from the modified Thomson-Cox-Hasting pseudo Voigt functions at the step i while n and p are the number of steps and parameters, respectively. The estimated values of the Rietveld R-factors and the goodness of fit index are listed in Table 2. Our results satisfied the requirement for a good refinement ($\chi^2 \geq 1$). The optimized fitted curves (Fig. 4) were used to

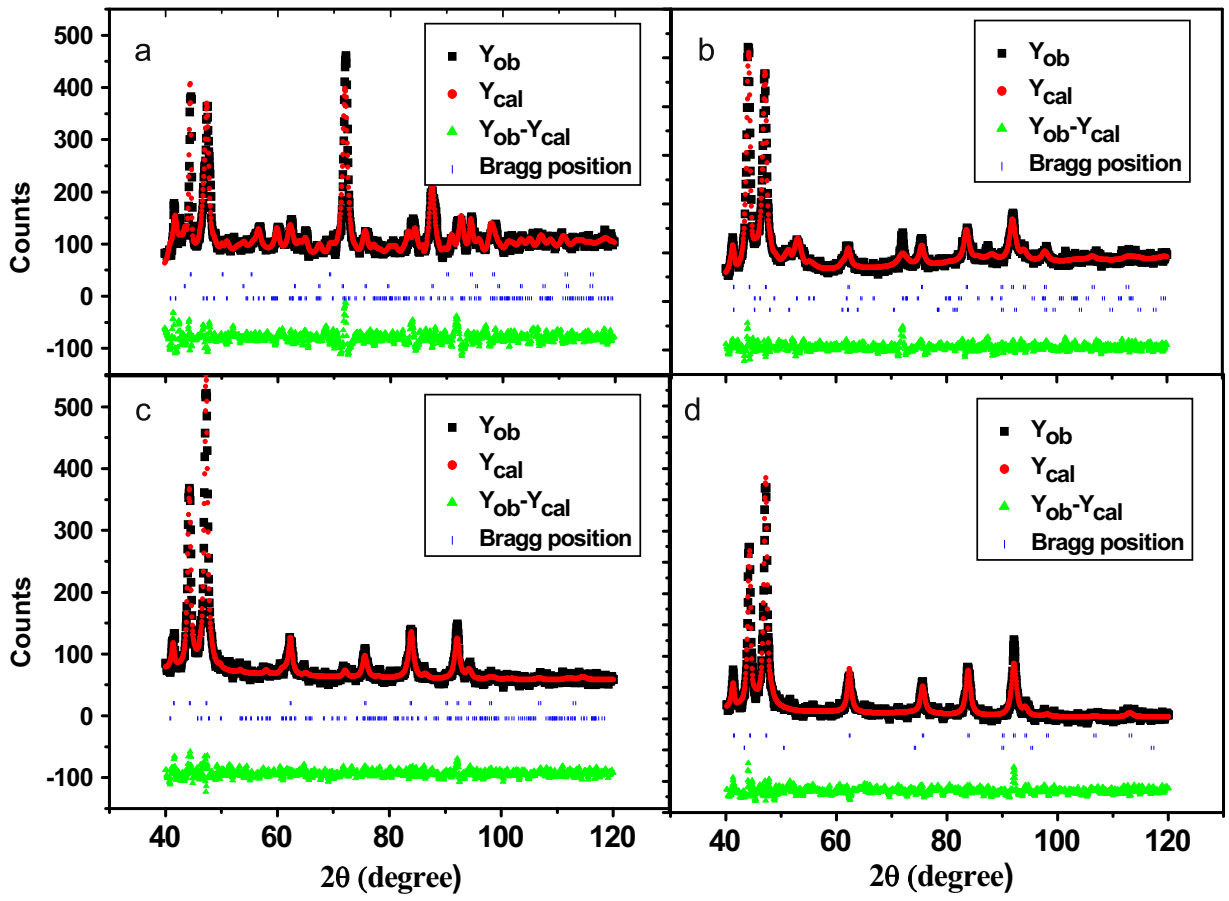

Fig. 4. Refined XRD profiles of Co–10 at% Cu alloys shown the observed peaks (Y_{ob}) by solid squares, the calculated peaks (Y_{cal}) by solid circles, the peak difference ($Y_{ob}-Y_{cal}$) by solid triangles and the corresponding Bragg's positions by vertical lines for sample (a) S1 (b) S2 (c) S3 (d) S4.

completely identify the phases, estimate the lattice parameter and quantify the crystal size of the samples.

The different phases present in the samples are summarized in Table 3. Co (phase 1) was present in all the samples. It has a hexagonal-close-packed (hcp) lattice structure at room temperature and a simple face center cubic (fcc) lattice structure at 1500 K since the annealing temperature was higher than 425 °C at which Co re-crystallizes and stabilizes with fcc structure (12). Due to thermal gradient, both hcp and fcc structures coexist in the samples. For example, Co (100) and Co (101) appeared as hcp structures at $2\theta=42^\circ$ and $2\theta=47^\circ$ respectively, while Co (220) has fcc structure at $2\theta=78^\circ$.

Table 3
Phases present in the samples obtained from FullProf software.

Sample	Phase 1	Phase 2	Phase 3	Phase 4
S1	Co	CuO	$CoCu_2O_3$	–
S2	Co	CuO	$CoCu_2O_3$	$CoCuO_2$
S3	Co	Cu	$CoCu_2O_3$	–
S4	Co	Cu	–	–

3.4. The lattice constants

The lattice constants, crystal systems and space groups for the different phases are depicted in Fig. 5. The changes in the lattice constants for the treated samples compared to the as-prepared sample showed that the crystal dimensions were affected by the thermal treatment. For the hcp crystal system, the ideal lattice constants are $a=2.514$ Å and $c=4.105$ Å as given in the ICDD cards [29]. The value of the lattice parameter 'a' shifted to a higher level for all the samples except S1 (Fig. 5a) that was aged for a shorter time. For the lattice parameter 'b', its value is lower for all the samples compared to the as-prepared sample. The lattice constant 'a' and 'b' for Cu/CuO-rich phase are slightly affected by the thermal process (Fig. 5b) while the thermal effect is less significant on the lattice parameters of $CoCu_2O_3$ phase (Fig. 5c). The observed shift in lattice constants can be due to either dissolved atoms or misfit inclusions [30].

By dissolving Cu atoms in the Co-rich phase, the additional Cu atoms increase the lattice parameter 'a' and decrease the lattice parameter of the Co-rich phase. Since the lattice constant for pure Cu is higher than the parameter 'a' of the pure Co, the Co crystal is strained in the direction of the lattice constant 'a', which is thereby elongated at the expense of the parameter 'c'. This shift was observed in Fig. 5a and was

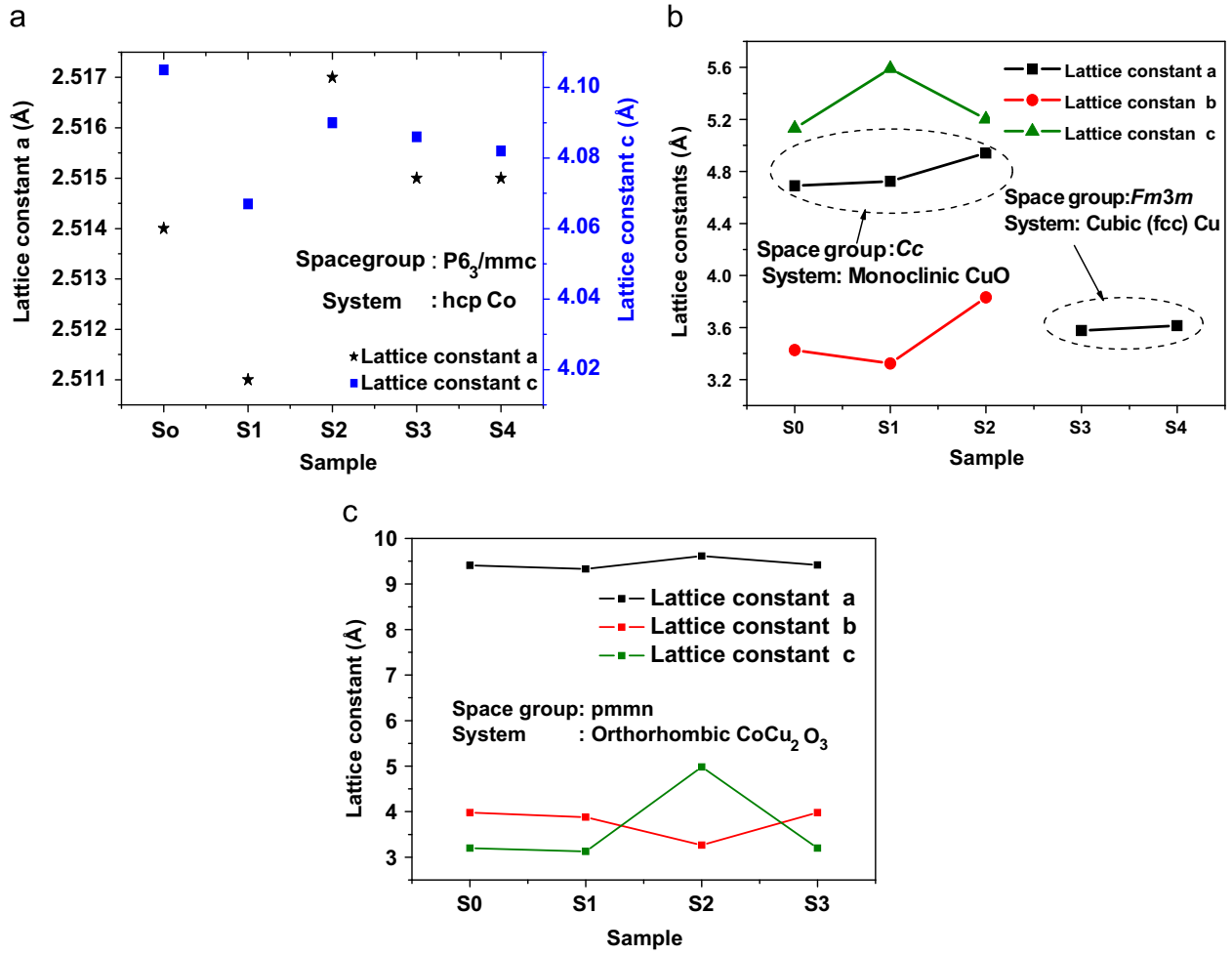

Fig. 5. Lattice constants and space group for phase (a) 1 (b) 2 and (c) 3. S0 is the reference sample (as-prepared). The continuous lines are guides to the eyes. The lattice constant for phase 4 shifted from 6.012 Å, for the as-prepared, to 5.95 Å after heat treatment.

proportional to the amount of dissolved atoms. For the Cu-rich phase, addition of Co atoms increased the lattice constant as observed for the fcc Cu (Fig. 5b). The parameters '*b*' and '*c*' of the CuO were also observed to have slightly increased. The movement of the Cu from the Cu-rich phase to the Co-rich phase was well observed in Fig. 2. The second reason for the observed shift in the lattice parameter is the misfit inclusion. This occurs when a multiphase alloy is subjected to temperature changes such as thermal treatment. In such a case, misfit stresses will be induced owing to the differences in the coefficients of thermal expansion of the phases. These misfit stresses include a hydrostatic component which changes the lattice parameters of both the matrix and the misfit inclusions [30]. This observation is similar to that of Vergara and Madurga [31].

3.5. Average grain size determination

The coherence length or crystal size *L* along a certain plane of a crystalline material can be calculated using the Scherrer formula [32].

$$L = \frac{K\lambda}{\beta \cos \theta} \tag{11}$$

where K is the Scherrer constant (generally taken as 1), β is the full width at half maximum (FWHM) in rad., λ is the wavelength of the X-ray and θ is the Bragg angle. The broadening of a diffraction peak is due to combined effects of in-plane crystallite size, lattice strain and instrumental broadening [33]. A correction for the instrumental broadening should be considered to obtain an accurate value of the grain size. If β in the Scherrer equation is actually β_{corr} which is the difference between the experimental broadening ($\beta_{exp.}$) and the instrumental broadening $\beta_{inst.}$, then Eq. (11) can be rewritten as follows:

$$\beta_{exp} = \left(\frac{K\lambda}{L}\right)\frac{1}{\cos \theta} + \beta_{inst} \tag{12}$$

If β_{inst} is constant within the measurement range, then Eq. (12) represents a straight line where β_{exp} is plotted against $1/\cos\theta$. The grain size L and the instrumental broadening β_{inst} are calculated from the slope of the resulting straight line.

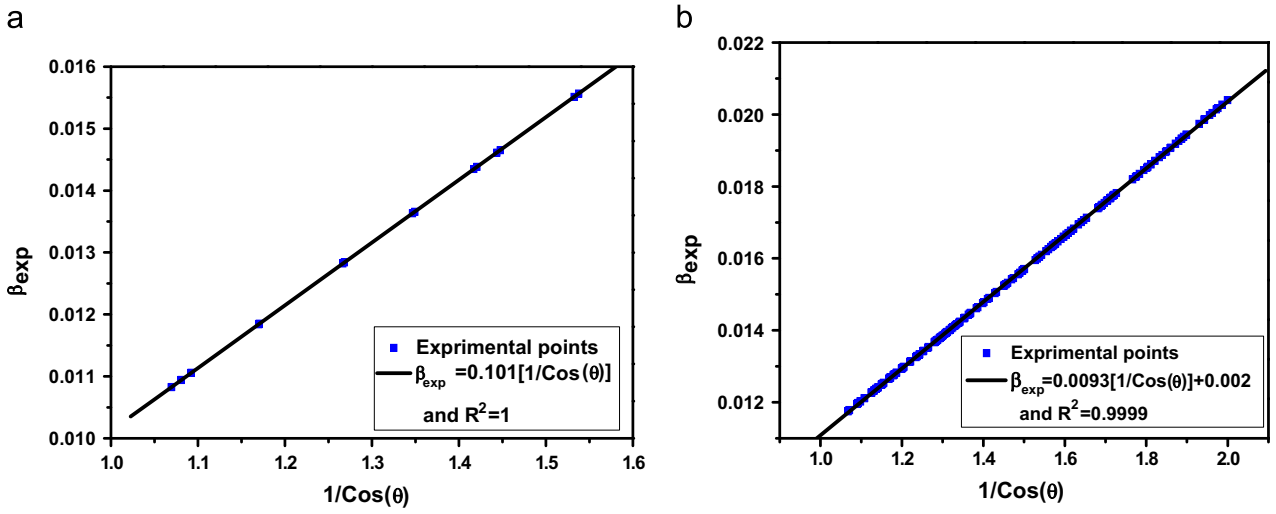

Fig. 6. Plots of β_{exp} against corresponding $(1/\cos\theta)$ for (a) phase 1, and (b) phase 3 of sample S1.

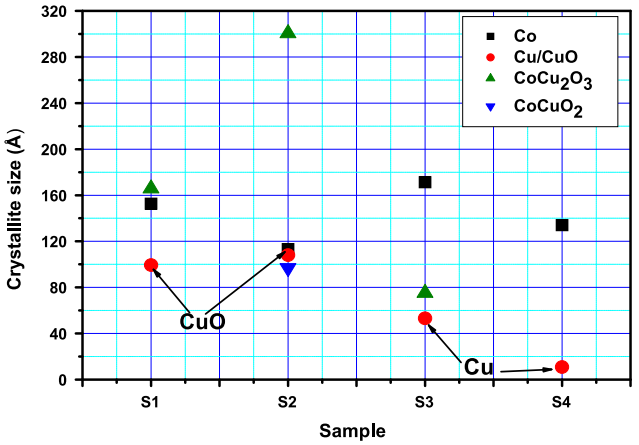

Fig. 7. Average crystallite size of the alloy′s phases estimated by Scherrer formula. The grid lines are guides to the eyes.

Graphical examples based on the modified Scherrer formula are shown in Fig. 6. High correlation coefficients (greater than 0.999) indicated that the data fitted excellently to the straight lines. β_{inst} for phase 1 and 3 of sample S1(see Fig. 6) were 0 and 0.0022, respectively indicating that instrumental broadening is negligible for phase 1 but not for phase 3. The grain size L can then be calculated for all the phases. As expected, the average grain size is both phase- and sample-dependant (Fig. 7). It was observed that the $CoCu_2O_3$ phase was one of the phases existing in the alloy and its crystallite size was dominant for S1 and S2. This is due to either high tendency of Cu and Co for oxidation or migration of Cu to Co-rich phase. The crystallite size for the Co phase is also significant and well favoured for S1, S3 and S4. The crystallite size of the Cu/CuO looks quite smaller.

4. Conclusions

The influence of thermal treatment on the phase decomposition and the grain size of Co–10 at% Cu alloys have been studied using EDS, SEM and XRD. EDS gives the fractional composition of the samples while XRD shows that the phase compositions in the alloys are Co, Cu, CuO, $CoCu_2O_3$, $CoCuO_2$. The proportion of each phase and the shifts in the refined lattice constants depend on heat treatment. The formation of the Cu oxide has profound effect on the occurrence of the spinodal decomposition. A correction for the instrumental broadening is considered and introduced in the Scherrer formula to obtain an accurate value of the grain size. The shifts in the refined lattice constants (*a, b* and *c*), the space group and the grain size were evaluated, and found to be phase- and heat treatment-dependant. 2D computer simulation indicates that the morphology and the shape of the precipitates agree with experimental observations. The elastic interaction energy among particles is essentially included in the present calculation. The interplay between the interfacial energy and the elastic energy is recognized in the system of Co–Cu to control the particles shape.

References

[1] A.M. Mebed, J.M. Howe, J. Appl. Phys. 100 (2006) 074310–074315.
[2] T. Fujita, S. Nishimura, T. Fujinami, K. Kaneko, Z. Horita, D.J. Smith, Mater. Sci. Eng. A 417 (2006) 149–157.
[3] H.B. Noh, K.S. Lee, P. Chandra, M.S. Won, Y.B. Shim, Electrochim. Acta 61 (2012) 36–43.
[4] A. Vannozzi, G. Thalmaier, A.A. Armenio, A. Augieri, V. Galluzzi, A. Mancini, A. Rufoloni, T. Petrisor, G. Celentano, Acta Mater. 58 (2010) 910–918.
[5] C.D. Cao, G.P. Görler, D.M. Herlach, B. Wei, Mater. Sci. Eng. A 325 (2002) 503–510.
[6] C.D. Cao, B. Wei, D.M. Herlach, J. Mater. Sci. Lett. 21 (2002) 341–343.
[7] J Gao, T Volkmann, J Strohmenger, D.M Herlach, Mater. Sci. Eng. A 520 (2004) 375–377.
[8] A.M. Mebed, M.I. Abd-Elrahman, A.M. Abd-Elnaiem, M.A. Gaffar, Phase Transit. 82 (2009) 587–598.
[9] A.M. Mebed, A.M. Abd-Elnaiem, T.B. Asafa, M.A. Gaffar, Phase Transit. 85 (2012) 1079–1090.
[10] A.M. Mebed, T. Koyama, T. Miyazaki, Comput. Mater. Sci. 14 (1999) 318–322.
[11] C.D. Cao, Z. Sun, X.J. Bai, L.B. Duan, J.B. Zheng, F. Wang, J. Mater. Sci. 46 (2011) 6203–6212.

[12] A.C. Zettlemoyer, Marcel Dekker, New York, 1969.
[13] M.I.M. Copetti, C.M. Elliott, Mater. Sci. Technol. 6 (1990) 273–284.
[14] D.A. Porter, K.E. Easterling, London, 1992.
[15] R.H. Yu, X.X. Zang, J. Tejada, M. Knobel, P Tibeto, P. Alliset, J. Appl. Phys 78 (1995) 392–397.
[16] R.A. Khan, A.S. Bhatti, J. Magn. Magn. Mater. 323 (2011) 340–345.
[17] H.M. Rietveld, J. Appl. Cryst. 2 (1969) 65–71.
[18] A. Le-Bail, H. Dwory, J.L. Fourquet, Mater. Res. Bull. 23 (1988) 447–452.
[19] G.S. Pawley, J. Appl. Crsyt. 14 (1981) 357–361.
[20] J.R. Carvajal, Physica B 192 (1993) 55–69.
[21] M.A. Gaffar, M.M. Ahmed, K. Yamada, T. Okuda, J. Phys. D: Appl. Phys. 40 (2007) 4360–4367.
[22] A.L. Ortiz, F.L. Cumbrera, F. Sánchez-Bajo, F. Guiberteau, H. Xu, N. P. Padture, J. Am. Ceram. Soc. 83 (2000) 2282–2286.
[23] A.G. Khachaturyan, John Willey, New York, NY, 1983.
[24] T. Koyama, T. Miyazaki, A.M. Mebed, Metall. Mater. Trans. A 26 (1995) 2617–2623.
[25] R.J. Graham, J.W. Steeds, J. Microscopy 133 (1984) 275–280.
[26] S.K. Eswaramoorthy, J.M. Howe, G. Muralidharan, Science 318 (2007) 1437–1440.
[27] J. Rodriguez-Carvajal, Laboratory Leon Brilloium (CEA-CNRS), 1997.
[28] P. Thompson, D.E. Cox, J.M. Hasting, J. Appl. Cryst. 20 (1987) 79–83.
[29] S. Heitmann, Cobalt/copper multilayers: interplay of microstructure and GMR and recrystallization as the key towards temperature stability, Bielefeld University, Bielefeld, 2004, p. 164 (Ph.D. thesis).
[30] M.J. Starink, V.M.F. Abeels, P. Van Mourik, Mater. Sci. Eng. A 163 (1993) 115–125.
[31] J. Vergara, V. Madurga, J. Phys.: Condens. Matter 14 (2002) 7513–7523.
[32] A.L. Patterson, Phys. Rev. 56 (1939) 978–982.
[33] N.C. Popa, D. Balzar, J. Appl. Cryst. 35 (2002) 338–346.